

Numerical Simulation of Underwater Explosions Using Unstructured Grids

Lingquan Li*, Rainald Löhner*, Facundo Nicolas Airaudó*
Corresponding author: lli32@ncsu.edu

* George Mason University, Fairfax, VA 22030, USA.

Abstract: The five-equation model for compressible two-phase flows has been extended to unstructured grids in order to model underwater explosions (UNDEX) close to complex geometries. The ideal equation of state (EOS) is used for air. The stiffened gas EOS is used for water. The Johnes-Wilkins-Lee (JWL) EOS is used for the high-explosive (HE) material to describe a simplified detonation process. A general formulation is written to include these different EOSs. A sharpening technique based on the hyperbolic tangent interpolation (THINC) is adopted to capture the transitioning interface. After verifying the accuracy of the numerical schemes against analytical and experimental results, ‘best practice guidelines’ have been developed to assure reliable results.

Keywords: Computational Fluid Dynamics, UNDEX, THINC limiter.

1 Introduction

Underwater explosions (UNDEX) have always been of interest for both military and civilian applications. The aim of the current work is to establish a mathematical model that is suitable for this class of problems. Any such model must take into account the three fluids that interact: air, water and HE.

Although a large body of work has been published for two-phase problems [1, 2, 3, 4, 5], publications for three fluids are less common, especially with HE. There have been studies for three fluids with the interface tracking method [6], but this method is limited to free-surface problems, e.g. an oil bubble rising in a partially filled container [6], making it unsuitable for flows with a large number of interfaces. This work aims to establish a simple and robust numerical method for UNDEX problems on vertex-centered unstructured grids [7]. This method is later extended to fluid-structure interaction problems [8].

The governing equation for the three-fluid model is a system of eight equations: the continuity and transport equation for air, water and HE material, respectively, the momentum and total energy equation for averaged flow. In this model, the pressure needs to be determined from a general formulation of EOS with mixed parameters. This numerical model is used for underwater explosions because of its simplicity and robustness. The spatial discretization is based on unstructured grids due to their flexibility to deal with complex geometries. An explicit multi-stage Runge-Kutta method is used for the temporal discretization. The interface

capturing method (THINC) [9, 10, 11, 12, 13] used for two-phase fluids is extended here to three-fluid problems.

2 Numerical Method

2.1 The Five-equation Model for Three-fluid Flows

The five-equation model for three-fluid flows may be written as

$$\frac{\partial z_1 \rho_1}{\partial t} + \nabla \cdot (z_1 \rho_1 \mathbf{u}) = 0, \quad (1)$$

$$\frac{\partial z_2 \rho_2}{\partial t} + \nabla \cdot (z_2 \rho_2 \mathbf{u}) = 0, \quad (2)$$

$$\frac{\partial z_3 \rho_3}{\partial t} + \nabla \cdot (z_3 \rho_3 \mathbf{u}) = 0, \quad (3)$$

$$\frac{\partial \rho \mathbf{u}}{\partial t} + \nabla \cdot (\rho \mathbf{u} \otimes \mathbf{u}) + \nabla p = \rho \mathbf{g}, \quad (4)$$

$$\frac{\partial \rho E}{\partial t} + \nabla \cdot [(\rho E + p) \mathbf{u}] = \rho \mathbf{g} \cdot \mathbf{u}, \quad (5)$$

$$\frac{\partial z_1}{\partial t} + \mathbf{u} \cdot \nabla z_1 = 0, \quad (6)$$

$$\frac{\partial z_2}{\partial t} + \mathbf{u} \cdot \nabla z_2 = 0, \quad (7)$$

$$\frac{\partial z_3}{\partial t} + \mathbf{u} \cdot \nabla z_3 = 0, \quad (8)$$

where

$$\rho = z_1 \rho_1 + z_2 \rho_2 + z_3 \rho_3, \quad (9)$$

and

$$\rho E = z_1 \rho_1 e_1 + z_2 \rho_2 e_2 + z_3 \rho_3 e_3 + \frac{1}{2} \rho \mathbf{u}^2 \quad (10)$$

are the averaged density and total energy, \mathbf{g} is the gravity acceleration, z_1 , z_2 and z_3 are the volume fractions of three fluids, respectively. It is notable that although there are eight equations in total, Eqn. 6, Eqn. 7 and Eqn. 8 are not independent from each other, since

$$z_1 + z_2 + z_3 = 1. \quad (11)$$

The volume fractions are re-scaled so that they add up to one whenever the solution is updated. The gravity effects are neglected in this paper unless specified. The Mie-Grüneisen EOS is used with the isobaric assumption to relate pressure to density and internal energy [14]. In the context, the subscript $k = 1$ is for the air, and $k = 2$ is for the liquid. The HE material is denoted with $k = 3$. Material densities are found from $(z_k \rho_k)/z_k$. The numerical errors become amplified due to the division by a very small volume fraction when $z_k \rightarrow 0$. A special treatment for the material densities is applied as

$$\rho_k = \begin{cases} z_k \rho_k / z_k, & \text{if } z_k > 10^{-6} \\ \epsilon_\rho, & \text{if } z_k \leq 10^{-6} \end{cases} \quad (12)$$

where ϵ_ρ is taken as 10^{-7} . The governing equations can be written as follows:

$$\frac{\partial \mathbf{U}}{\partial t} + \frac{\partial \mathbf{F}_j}{\partial x_j} = \mathbf{S}, \quad (13)$$

where

$$\mathbf{U} = \begin{bmatrix} z_1 \rho_1 \\ z_2 \rho_2 \\ z_3 \rho_3 \\ \rho u_i \\ \rho E \\ z_1 \\ z_2 \\ z_3 \end{bmatrix}, \quad \mathbf{F}_j = \begin{bmatrix} z_1 \rho_1 u_j \\ z_2 \rho_2 u_j \\ z_3 \rho_3 u_j \\ \rho u_i u_j + p \delta_{ij} \\ (\rho E + p) u_j \\ z_1 u_j \\ z_2 u_j \\ z_3 u_j \end{bmatrix}, \quad \mathbf{S} = \begin{bmatrix} 0 \\ 0 \\ 0 \\ \rho g_i \\ \rho \mathbf{g} \cdot \mathbf{u} \\ z_1 \frac{\partial u_j}{\partial x_j} \\ z_2 \frac{\partial u_j}{\partial x_j} \\ z_3 \frac{\partial u_j}{\partial x_j} \end{bmatrix}. \quad (14)$$

2.2 Mie-Grüneisen General Form of EOS

To close system Eqn. 1-Eqn. 8, the relation between internal energy, pressure and density is needed. The ideal gas EOS is used for air:

$$p_1 = (\gamma_1 - 1) \rho_1 e_1, \quad (15)$$

where $\gamma_1 = 1.4$. The stiffened gas EOS is used for water:

$$p_2 = (\gamma_2 - 1) \rho_2 e_2 - \gamma_2 P_c. \quad (16)$$

where $\gamma_2 = 4.4$ and $P_c = 6.0 \times 10^8 Pa$. The Jones-Wilkins-Lee (JWL) EOS is used for the HE:

$$p = A \left(1 - \frac{\omega}{R_1 V}\right) e^{-R_1 V} + B \left(1 - \frac{\omega}{R_2 V}\right) e^{-R_2 V} + \omega \rho e, \quad (17)$$

where V is the relative volume of the HE gas.

$$V = \frac{\rho_0}{\rho}. \quad (18)$$

The properties of TNT are given in Table 1.

Table 1: JWL EOS parameters for High Explosive Materials

Property	TNT
$A(GPa)$	371.20
$B(GPa)$	3.231
R_1	4.15
R_2	0.95
ω	0.30
$e_0(m^2/s^2)$	4.2945×10^6
$\rho_0(kg/m^3)$	1.630×10^3
$v_d(m/s)$	6930.0

Mie-Grüneisen formulation EOS gives a general representation of complex equations of state

[14]:

$$\begin{aligned} p_k(\rho_k, e_k) &= \Gamma_k(\rho_k)\rho_k e_k + \beta_k(\rho_k) \\ &= \Gamma_k(\rho_k)\rho_k e_k + p_{ref}(\rho_k) - \Gamma_k(\rho_k)\rho_k e_{ref}(\rho_k). \end{aligned} \quad (19)$$

Table 2: Parameters to obtain equivalent Mie-Grüneisen EOS form

	$\Gamma(\rho)$	$p_{ref}(\rho)$	$e_{ref}(\rho)$
Ideal gas	$\gamma_1 - 1$	0	0
Stiffened gas	$\gamma_2 - 1$	$-\gamma_2 P_c$	0
JWL	ω	$Ae^{-R_1 V} + Be^{-R_2 V}$	$\frac{A}{\rho_0 R_1} e^{-R_1 V} + \frac{B}{\rho_0 R_2} e^{-R_2 V} - e_0$

2.3 Speed of Sound

With the general Mie-Grüneisen form of EOS, the speed of sound can be obtained as:

$$c_k^2(\rho_k, p) = \left(\Gamma_k + 1 + \rho_k \frac{\Gamma'_k}{\Gamma_k} \right) \left(\frac{p - (p_{ref})_k}{\rho_k} \right) + \Gamma_k \frac{(p_{ref})_k}{\rho_k} + (p'_{ref})_k - \Gamma_k \rho_k (e_{ref})'_k, \quad (20)$$

where Γ' , p'_{ref} and e'_{ref} are derivatives of the EOS functions with respect to ρ .

2.4 Mixing Parameters

The mixing strategy is performed on the function

$$\beta_k(\rho_k) = p_{ref}(\rho_k) - \Gamma_k(\rho_k)\rho_k e_{ref}(\rho_k), \quad (21)$$

and $\Gamma_k(\rho_k)$. The averaging parameters are

$$\xi_k(\rho_k) = \frac{1}{\Gamma_k(\rho_k)}, \quad (22)$$

and

$$\xi = \sum_k z_k \xi_k(\rho_k). \quad (23)$$

Applying the mixing parameters to average $\Gamma_k(\rho_k)$ and $\beta_k(\rho_k)$ with the isobaric assumption, the pressure and total internal energy for the mixture are found from

$$p(\rho_k, \rho e, z_k) = \frac{1}{\xi} \left[\rho e + \sum_k z_k \xi_k(\rho_k) \beta_k(\rho_k) \right], \quad (24)$$

and

$$\rho e = \xi p - \sum_k z_k \xi_k(\rho_k) \beta_k(\rho_k). \quad (25)$$

A mixed speed of sound is evaluated as

$$c^2 = \frac{1}{\xi} \sum_k y_k \xi_k c_k^2, \quad (26)$$

where the mass fraction is $y_k = z_k \rho_k / \rho$.

2.5 Spatial Discretization

The three fluid system is discretized with the finite volume method. If the computational domain Ω is composed of control volumes Ω_e , and the boundaries of Ω_e are denoted as Γ_e , then the integration over each control volume gives the semi-discrete form:

$$\int_{\Omega_e} \frac{\partial \mathbf{U}_k}{\partial t} d\Omega + \int_{\Gamma_e} (\mathbf{F}_k \cdot \mathbf{n}) d\Gamma = \int_{\Omega_e} \mathbf{S}_k d\Omega, \quad (27)$$

where \mathbf{n} is the outwards unit vector normal to Γ_e . Kuzmin's VB limiter is first applied to a set of primitive variables $\mathbf{W} = [z_k, \rho_k, \mathbf{u}, p]$, and the THINC method is applied to z_k only at the transitioning phase. This process is described in [12]. It should be remarked that z_k needs to be re-scaled according to the constraint (11).

2.6 Temporal Discretization

If all the temporal derivatives are moved to the left hand side in equation (13), then equation (27) can be rewritten as

$$\int_{\Omega_e} \frac{\partial \mathbf{U}_k}{\partial t} d\Omega = \mathbf{R}_k. \quad (28)$$

The following explicit forward Euler method is used:

$$\begin{aligned} \hat{\mathbf{U}}_k^{(1)} &= \hat{\mathbf{U}}_k^n + \frac{\Delta t}{V_e} \mathbf{R}_k^n, \\ \hat{\mathbf{U}}_k^{(2)} &= \frac{3}{4} \hat{\mathbf{U}}_k^n + \frac{1}{4} \left(\hat{\mathbf{U}}_k^{(1)} + \frac{\Delta t}{V_e} \mathbf{R}_k^{(1)} \right), \\ \hat{\mathbf{U}}_k^{n+1} &= \frac{1}{3} \hat{\mathbf{U}}_k^n + \frac{2}{3} \left(\hat{\mathbf{U}}_k^{(2)} + \frac{\Delta t}{V_e} \mathbf{R}_k^{(2)} \right), \end{aligned} \quad (29)$$

where V_e is the volume of the considered element, and Δt is the time step. For all examples shown the CFL number is taken as 0.6 unless otherwise noted.

3 Numerical Results

3.1 Manufactured Steady Problem of Mixed Air and Water

The one-dimensional manufactured steady problem of air and water is given to study the accuracy of the numerical method. The air and water are mixed smoothly, instead of dominated by interface problem. Therefore, the sharpening technique is not activated. The primitive variables are assumed to be distributed smoothly as:

$$\begin{cases} z_1 = A_z + B_z \sin(2\pi x), \\ z_2 = 1.0 - A_z - B_z \sin(2\pi x), \\ \rho_1 = A_{\rho_1} + B_{\rho_1} \sin(2\pi x), \\ \rho_2 = A_{\rho_2} + B_{\rho_2} \sin(2\pi x), \\ u = A_u + B_u \cos(2\pi x), \\ p = A_p + B_p \cos(2\pi x). \end{cases} \quad (30)$$

Since the solution is supposed to be steady, all the time derivatives should be zero once the solution is converged. To get the steady manufactured solution, the source terms need to be

introduced as

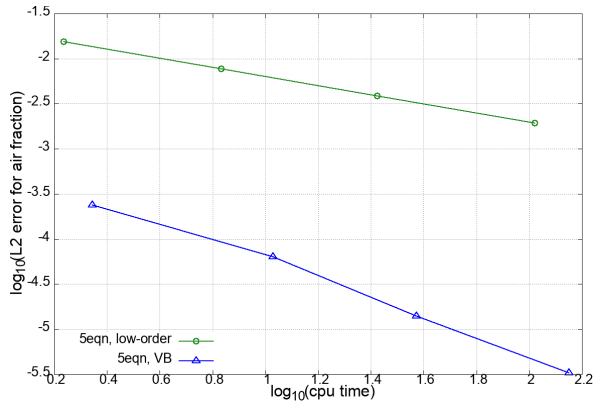
$$\left\{ \begin{array}{l} \nabla \cdot (z_1 \rho_1 \mathbf{u}) = (\rho_1 u) \frac{\partial z_1}{\partial x} + (z_1 u) \frac{\partial \rho_1}{\partial x} + (z_1 \rho_1) \frac{\partial u}{\partial x}, \\ \nabla \cdot (z_2 \rho_2 \mathbf{u}) = (\rho_2 u) \frac{\partial z_2}{\partial x} + (z_2 u) \frac{\partial \rho_2}{\partial x} + (z_2 \rho_2) \frac{\partial u}{\partial x}, \\ \nabla \cdot (\rho \mathbf{u} \otimes \mathbf{u}) + \nabla p = (u^2) \frac{\partial \rho}{\partial x} + 2\rho u \frac{\partial u}{\partial x} + \frac{\partial p}{\partial x}, \\ \nabla \cdot [(\rho E + p) \mathbf{u}] = \frac{\partial}{\partial x} \left[\left(p + z_1 \frac{p}{\gamma_1 - 1} + z_2 \frac{p + \gamma_2 P_c}{\gamma_2 - 1} + \frac{1}{2} \rho u^2 \right) u \right], \\ \mathbf{u} \cdot \nabla z_1 = u \frac{\partial z_1}{\partial x}. \end{array} \right. \quad (31)$$

These source terms can be derived from Eqn. 30. The parameters in Eqn. 30 are given as

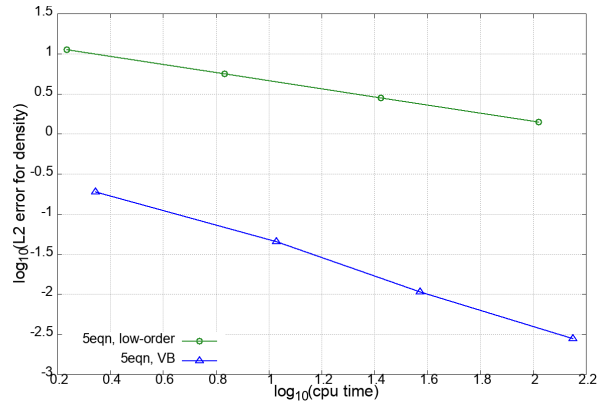
$$\left\{ \begin{array}{l} A_z = 0.5, \\ B_z = 0.2, \\ A_{\rho_1} = 1.225, \\ B_{\rho_1} = 0.1225, \\ A_{\rho_2} = 1000.0, \\ B_{\rho_2} = 100.0, \\ A_u = 100.0, \\ B_u = 10.0, \\ A_p = 1.01325 \times 10^5, \\ B_p = 1.01325 \times 10^4. \end{array} \right. \quad (32)$$

The computational domain is taken as $0.0m \leq x \leq 1.0m$. The mesh is consecutively refined with total number of nodes as 51, 101, 201 and 401 to study the accuracy of the numerical method. The CFL number is taken as 0.2, and the solution is taken as convergent when the relative residual reaches 1.0×10^{-5} for the considered cell size.

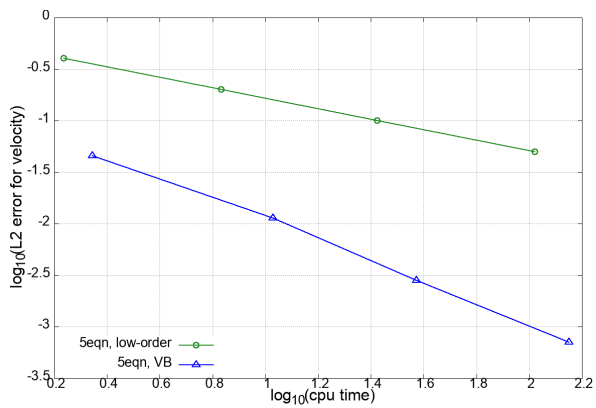
The computational efficiency and accuracy study is shown in Fig. 1 and Fig. 2. From Fig. 1, one can see that the L2 error converges faster with the VB scheme than with the low-order scheme. The order of accuracy is shown in Fig. 2, from where one can see that the 'low-order' method converges to first-order accuracy, while the 'VB' method converges to second-order accuracy for the manufactured smooth solution.



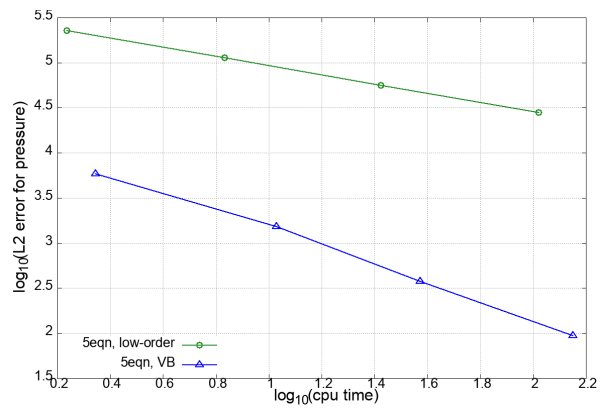
(a) L2 error for z_1 against CPU time



(b) L2 error for ρ against CPU time



(c) L2 error for u against CPU time



(d) L2 error for p against CPU time

Figure 1: CPU efficiency analysis for air-water manufactured solution

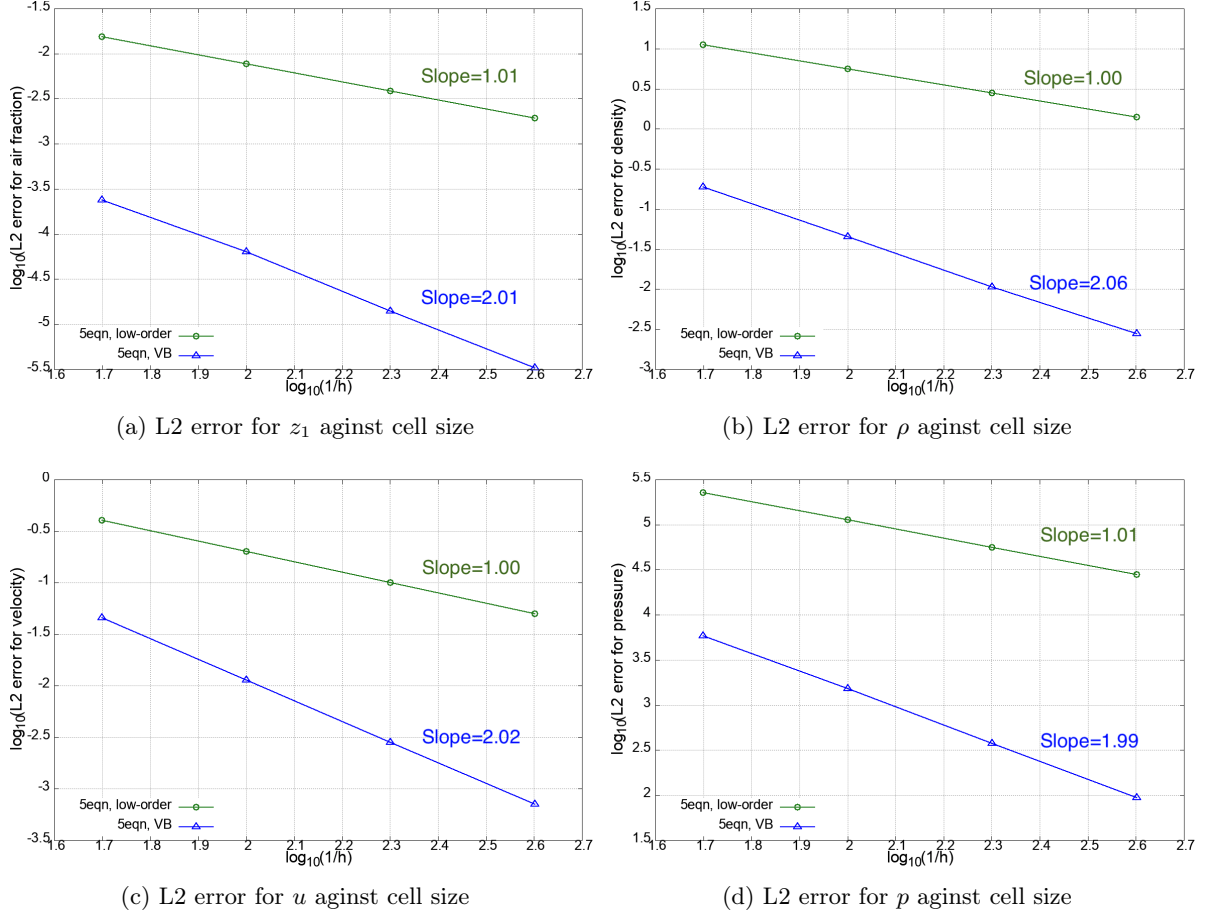


Figure 2: Accuracy analysis for air-water manufactured solution

3.2 Air-water Shock Tube

The one-dimensional shock tube is filled with air under high pressure at the left ($0.0m \leq x \leq 0.5m$), and with water under atmospheric pressure at the right ($0.5m < x \leq 1.0m$). The initial conditions are given as follows:

$$\begin{pmatrix} z_1 \\ p \\ u \\ T \end{pmatrix}_L = \begin{pmatrix} 1.0 \\ 10^9 Pa \\ 0.0m/s \\ 308.15K \end{pmatrix}, \quad \begin{pmatrix} z_1 \\ p \\ u \\ T \end{pmatrix}_R = \begin{pmatrix} 0.0 \\ 10^5 Pa \\ 0.0m/s \\ 308.15K \end{pmatrix}. \quad (33)$$

The EOS parameters used here are slightly different as: $\gamma_1 = 1.4$, $\gamma_2 = 2.8$ and $P_c = 8.5 \times 10^8 Pa$. The specific heat capacity for air and water is $1004.5 J/(kg \cdot K)$ and $4186 J/(kg \cdot K)$ respectively. The results converge to the exact solution from in terms of air fraction, velocity and pressure.

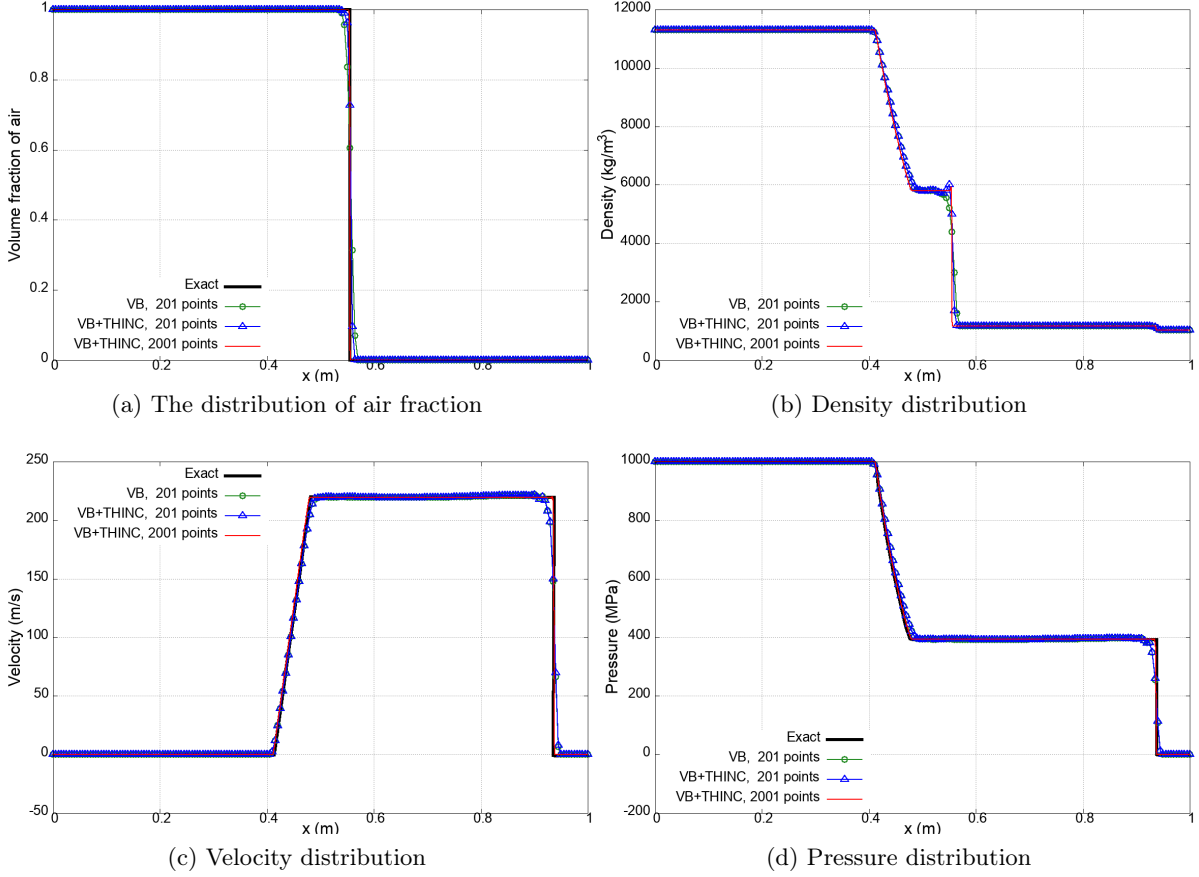


Figure 3: Air-water shock tube with $p_L/p_R = 10^4$ at time of $2.5 \times 10^{-4}s$

3.3 TNT Ignition in Water

This example shows the initial ignition process of TNT in water. The ignition is simplified because the 'simplest theory' of detonation model is adopted in this paper. However, it gives the information after the ignition, and later can be used as initial conditions for UNDEX problem. The computation domain is taken as $0.0cm \leq r \leq 20.7cm$, $0^\circ \leq \theta \leq 15^\circ$ and $75^\circ \leq \phi \leq 90^\circ$ in spherical coordinate system. The mesh shown in Fig. 4 is composed of 1,722,741 elements, 304,481 nodes, and 29,025 boundary points. The domain is filled with water, and 1kg of TNT product is put at the spherical center. The atmospheric pressure is given for initialization, then the ignition begins at the origin.

The 'VB' and 'VB+THINC' methods are compared in Fig. 5. The 'VB' method gives a diffusive interface after $20\mu s$, while 'VB+THINC' is able to keep the sharp interface. The pressure field is given in Fig. 6 in *cgs* unit. At time of $5\mu s$, a high-pressure shock wave is transmitted into the TNT material. This shock wave reaches the TNT-water interface. Due to the over expansion of the TNT, the pressure at the explosion core drops quickly. After the expansion, a high-pressure field is formed at the spherical center at time of $15\mu s$. At time of $20\mu s$, the high-pressure wave at the spherical center is going to the outer field again, while the first shock wave is much weakened. At time of $25\mu s$, the high-pressure field at the center keeps pushing the TNT-water interface, and enhances the shock wave across the interface. This shock wave keeps going into the water as can be seen at time of $35\mu s$ and $50\mu s$.

The efficiency of parallelism is studied for this test case in Tab. 3 for both the 'VB' and 'VB+THINC' methods. It can be seen that the elapsed time for computation is inversely

proportional to the number of processors. This demonstrates that the present methods are efficient in terms of parallel computing. The table also shows how the addition of THINC adds some computational overhead. However, this difference becomes almost negligible as we run in parallel.

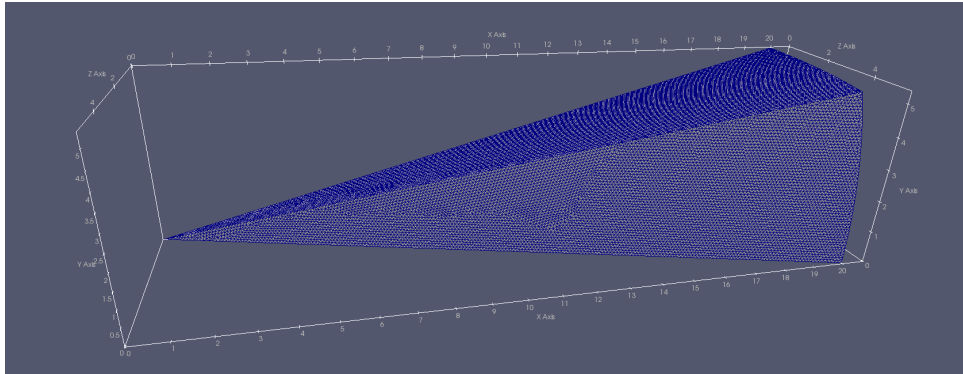


Figure 4: Mesh for TNT ignition in water

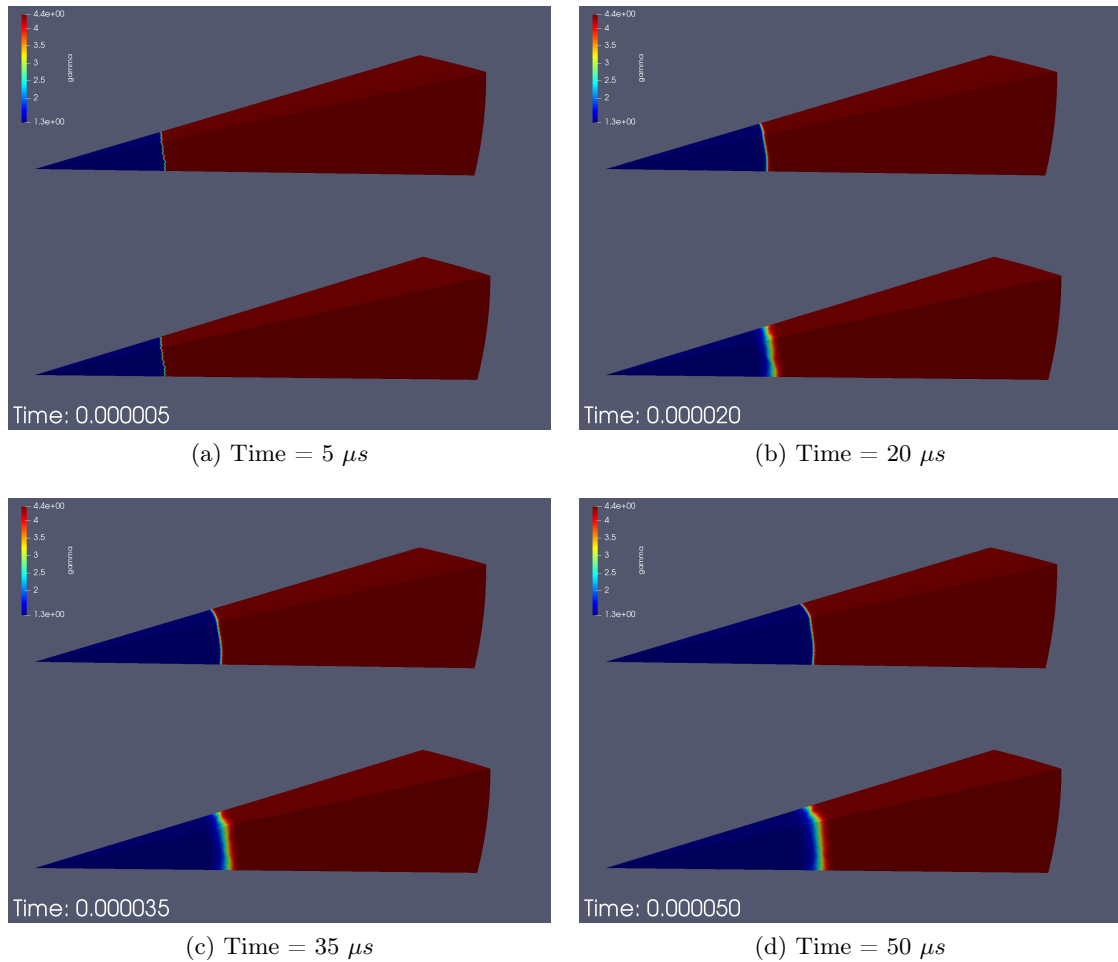


Figure 5: γ for TNT ignition in water (Upper: VB+THINC; Lower: VB)

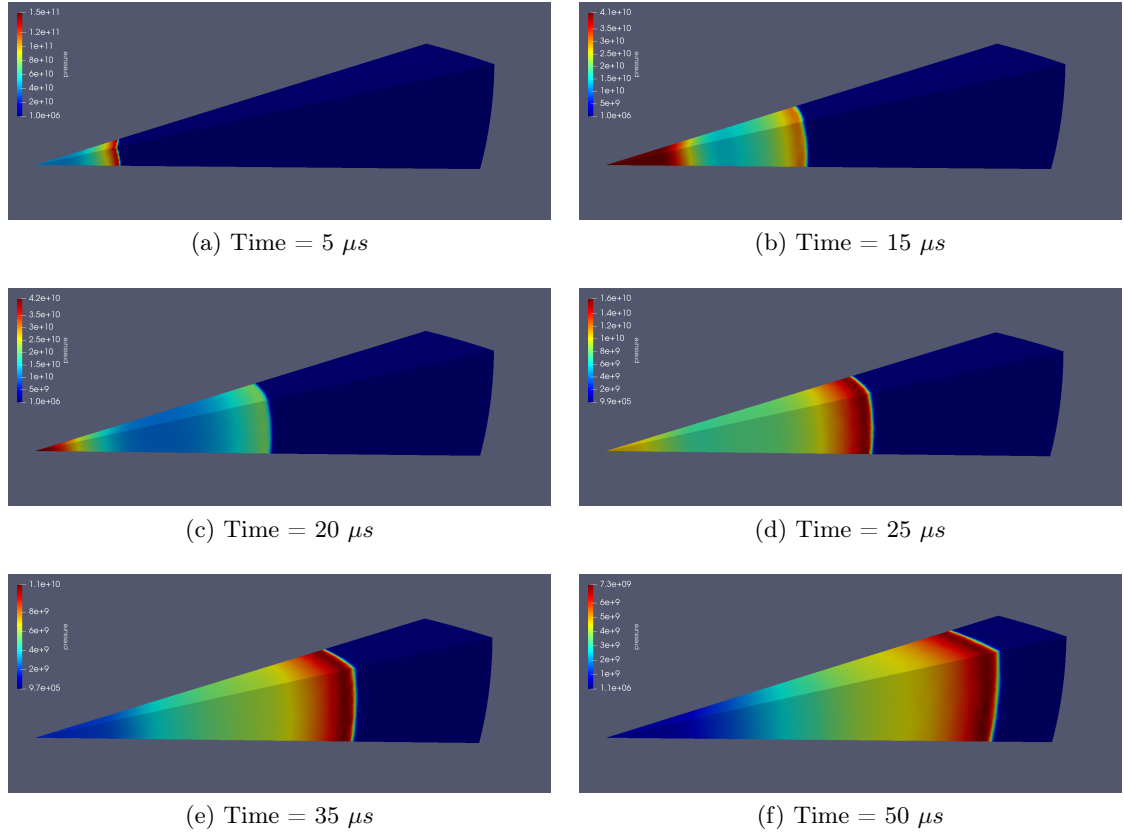


Figure 6: Pressure (Ba) for TNT ignition in water

Table 3: Efficiency of parallelism for TNT ignition in water

Number of processors	1	2	4	8	16
VB Elapsed time (s)	3457	1840	985	597	383
VB+THINC Elapsed time (s)	3863	1974	1096	656	412

3.4 UNDEX Near a Rigid Cylinder in a Tank Partially Filled with Water

An UNDEX near a rigid cylinder column is shown as a generic three-fluid problem. A rigid cylinder column with a diameter of $15in$ ($38.1cm$) and a height of $7.0m$ is fixed in a tank partially filled with water. The depth of water is $5.0m$, and the water surface is set as $y = 0.0m$. A TNT charge of $1.0kg$ is put $2.5m$ under the water surface, with a stand-off distance of $0.50m$ from the column surface. The mesh is composed of 65 million tetrahedral elements. The mesh is further refined at the water surface, near the column and at the TNT charge position. To compare the present numerical method with the empirical equations, the mesh is refined to the size of $0.20cm$ at two specific locations horizontal to the explosion center, as shown in Fig. 7. The free-field station is in the free-field water, $50cm$ away from the detonation center. The other station is exactly at the column surface facing the explosion.

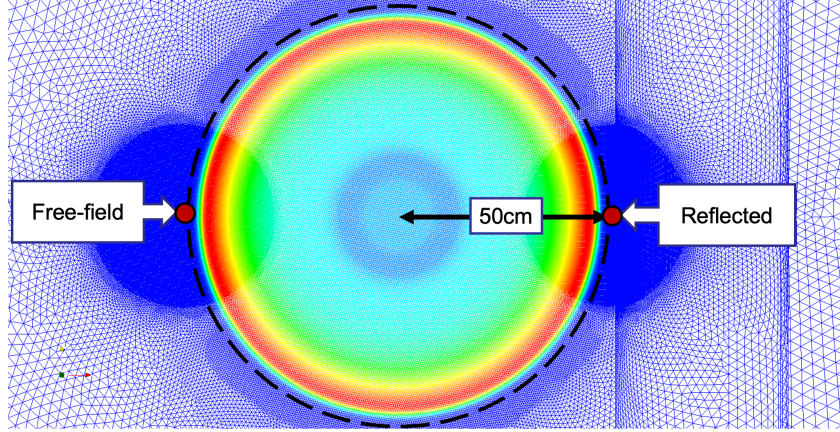


Figure 7: Free-field station and reflected station at 0.5cm for UNDEX near a rigid cylinder column in a tank partially filled with water, colored with pressure

Table 4: Comparison with empirical equations for UNDEX near a slender cylinder column (TNT charge of 1kg ; stations 50cm away from the explosion center)

	Present method	Cole's	Zhuang's
Free-field pressure (Pa)	1.25×10^8	1.15×10^8	–
Free-field impulse ($Pa \cdot s$)	1.67×10^4	1.07×10^4	–
Reflected pressure (Pa)	2.56×10^8	–	–
Reflection coefficient	2.05	–	2.40

3.5 UNDEX Near a Steel Plate

This test case is taken from [15] and considers an UNDEX near a submerged, end-clamped circular steel plate. The flow characteristics and structural response of the steel structure subjected to the UNDEX are studied. The steel plate's density, Young's modulus, Poisson's rate and yield strength are chosen as $\rho_s = 8000\text{kg/m}^3$, $E_s = 2.1 \times 10^{11}\text{Pa}$, $\mu_s = 0.27$ and $\sigma_s = 9.0 \times 10^8\text{Pa}$, respectively. The thickness of the steel plate is 6.8cm . The initial radius, density and pressure of the bubble are set to be 0.5m , 1630kg/m^3 and 6.0GPa . The initial density and pressure for water are set as 1000kg/m^3 and 10^5Pa . The pressure gradient contours and pressure contours at time of 0.0ms , 0.1ms , 0.5ms , 1.0ms , 1.5ms , 2.0ms , 2.5ms and 3.0ms are shown in Fig. 8 and Fig. 9.

4 Conclusion and Future Work

The numerical example shown and others that have been recently run demonstrate that the present method is simple to be implemented, accurate, efficient and robust. The results agree well with the empirical equations. The numerical method is then further extended to underwater explosions with more realistic fluid-structure interactions. Future study can be focused on the improvement of the cavitation model.

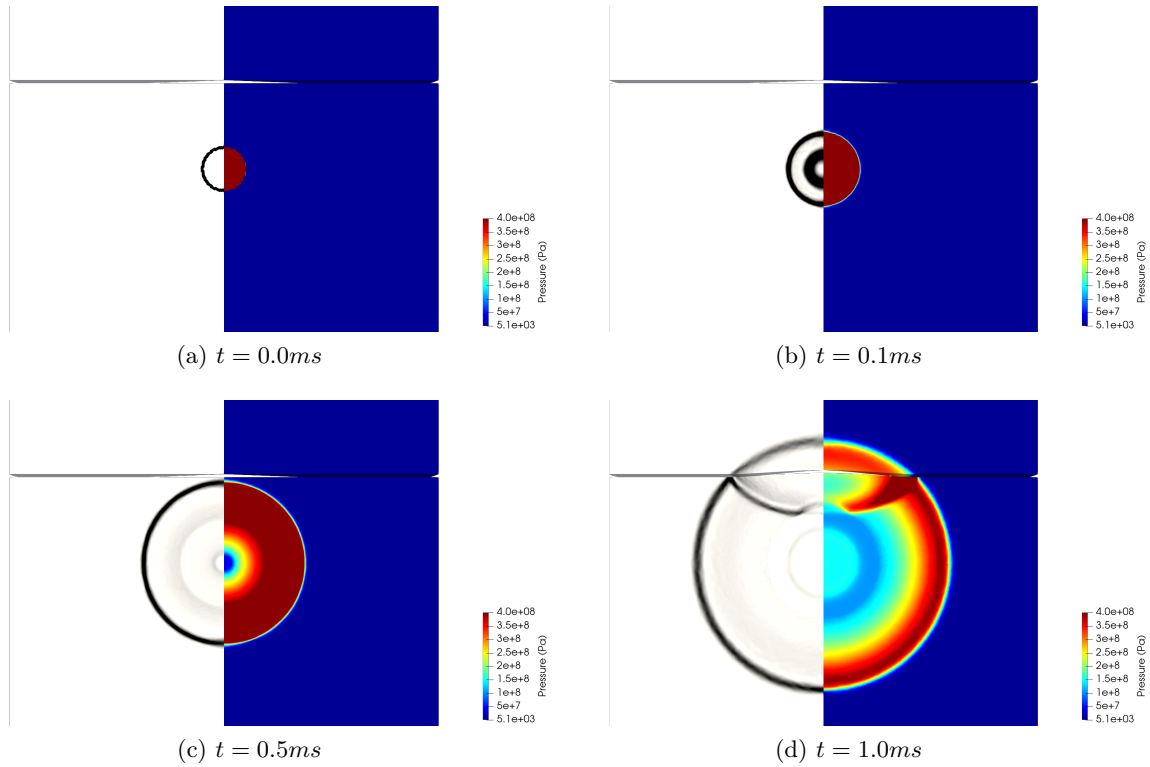


Figure 8: Pressure gradient contours (left) and pressure contours (right) for UNDEX near a steel plate at $0.0ms$, $0.1ms$, $0.5ms$ and $1.0ms$

References

- [1] G.-S. Yeom, K.-S. Chang, A modified hllc-type riemann solver for the compressible six-equation two-fluid model, *Computers & Fluids* 76 (2013) 86–104.
- [2] L. Zou, H. Zhao, H. Zhang, Implicitly solving phase appearance and disappearance problems using two-fluid six-equation model, *Progress in Nuclear Energy* 88 (2016) 198–210.
- [3] G. Hu, T. Kozłowski, A roe-type numerical solver for the two-phase two-fluid six-equation model with realistic equation of state, *Nuclear Engineering and Design* 326 (2018) 354–370.
- [4] S. Liang, W. Liu, L. Yuan, Solving seven-equation model for compressible two-phase flow using multiple gpus, *Computers & Fluids* 99 (2014) 156–171.
- [5] A. K. Pandare, H. Luo, A robust and efficient finite volume method for compressible inviscid and viscous two-phase flows, *Journal of Computational Physics* 371 (2018) 67–91.
- [6] R. Yang, H. Li, A. Yang, A hllc-type finite volume method for incompressible two-phase flows, *Computers & Fluids* 213 (2020) 104715.
- [7] L. Li, R. Lohner, A. Pandare, H. Luo, Numerical modeling for compressible three-fluid flows with high explosive material, in: *AIAA AVIATION 2021 FORUM*, 2021, p. 2858.
- [8] L. Li, R. Lohner, O. A. Soto, J. D. Baum, Numerical modeling of underwater explosion with fluid-structure interaction, in: *AIAA SCITECH 2022 Forum*, 2022, p. 0352.

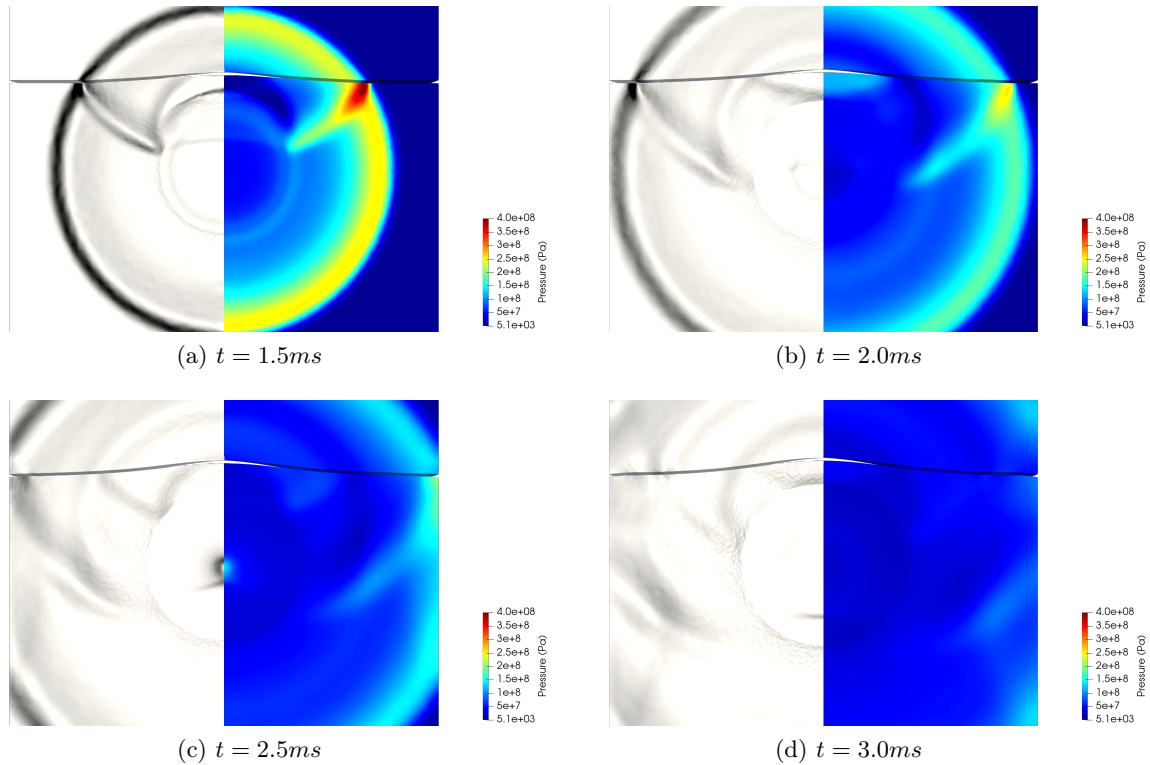


Figure 9: Pressure gradient contours (left) and pressure contours (right) for UNDEX near a steel plate at $1.5ms$, $2.0ms$, $2.5ms$ and $3.0ms$

- [9] R. K. Shukla, C. Pantano, J. B. Freund, An interface capturing method for the simulation of multi-phase compressible flows, *Journal of Computational Physics* 229 (19) (2010) 7411–7439.
- [10] T. Bonometti, J. Magnaudet, An interface-capturing method for incompressible two-phase flows. validation and application to bubble dynamics, *International Journal of Multiphase Flow* 33 (2) (2007) 109–133.
- [11] S. Mirjalili, S. S. Jain, M. Dodd, Interface-capturing methods for two-phase flows: An overview and recent developments, *Center for Turbulence Research Annual Research Briefs 2017* (2017) 117–135.
- [12] L. Li, R. Lohner, A. Pandare, H. Luo, A vertex-centered finite volume method with sharp interface capturing for compressible two-phase flows, in: *AIAA Scitech 2021 Forum*, 2021, p. 0856.
- [13] L. Li, R. Löhner, A. K. Pandare, H. Luo, A vertex-centered finite volume method with interface sharpening technique for compressible two-phase flows, *Journal of Computational Physics* 460 (2022) 111194.
- [14] M. A. Price, V.-T. Nguyen, O. Hassan, K. Morgan, A method for compressible multia-material flows with condensed phase explosive detonation and airblast on unstructured grids, *Computers & Fluids* 111 (2015) 76–90.

- [15] L. Ge, A.-M. Zhang, S.-P. Wang, Investigation of underwater explosion near composite structures using a combined rkdg-fem approach, *Journal of Computational Physics* 404 (2020) 109113.